Final Report: Molecular Mechanisms of Interfacial Reactivity in Near Surface and Extreme Geochemical Environments (DE-SC0009362)

David A. Dixon, Department of Chemistry, The University of Alabama

The prediction of the long-term stability and safety of geologic sequestration of greenhouse gases requires a detailed understanding of subsurface transport and chemical interactions between the disposed greenhouse gases and the geologic media. In this regard, mineral-fluid interactions are of prime importance since reactions that occur on or near the interface can assist in the long term sequestration of CO_2 by trapping in mineral phases such as carbonates, as well as influencing the subsurface migration of the disposed fluids via creation or plugging of pores or fractures in the host rock strata. Previous research on mineral-fluid interaction for subsurface CO_2 storage has focused almost entirely on the aqueous phase, i.e., reactivity with aqueous solutions or brines containing dissolved CO_2. However, interactions with neat to water-saturated non-aqueous fluids are of equal if not greater importance since supercritical CO_2 (scCO_2) is less dense than the aqueous phase or oil which will create a buoyant scCO_2 plume that ultimately will dominate the pore volume within the caprock, and the injected scCO_2 will contain water soon after injection and this water can be highly reactive. Collectively, therefore, mineral interactions with water-saturated scCO_2-dominated fluids are pivotal and could result in the stable sequestration of CO_2 by trapping in mineral phases such as metal carbonates within otherwise permeable zones in the caprock. The primary objective is to unravel the molecular mechanisms governing the reactivity of mineral phases important in the geologic sequestration of CO_2 with variably wet supercritical carbon dioxide as a function of T, P, and mineral structure using computational chemistry. This work is in close collaboration with the PNNL Geosciences effort. The focus of the work at The University of Alabama is computational studies of the formation of magnesium and calcium carbonates and oxides and their reactivity and providing computational support of the experimental efforts at PNNL, especially for energetics, structural properties, and interpretation of spectra.

Complexation of the Uranyl Dication with Anionic Phosphate Ligands with and without Water Molecules

Phosphates and their derivatives $((RO)_3PO)$, R = H, alkyl, phenyl) form one of the most important classes of ligands in actinide chemistry. Mineralization has been considered as an approach to produce actinide phosphates as matrices for long-term radioactive waste storage. Biological organisms can accumulate and precipitate uranyl ions from the environment. EXAFS measurements of the nature of the uranyl complexes formed at the surfaces of *Bacillus cereus* and *Bacillus sphaericus* cells and spores showed that uranium binding primarily occurs at the phosphoryl residues on the cell walls of these Gram-positive residues, mainly in a monodentate fashion. It was suggested that lipopolysacharides and phospholipids within the bacterial cell wall can also provide phosphoryl groups for metal ion binding. The structures, vibrational frequencies and energetics of anhydrous and hydrated complexes of UO_2^{2+} with the phosphate anions $H_2PO_4^-$, HPO_4^{2-}, and PO_4^{3-} were predicted at the density functional theory (DFT) and MP2 molecular orbital theory levels as isolated gas phase species and in aqueous solution by using self-consistent reaction field (SCRF) calculations with different solvation models.

The geometries, and vibrational frequencies of the major binding modes for these complexes are compared to experiment where possible and good agreement is found. Adequate steric space is available in these complexes to accommodate multiple water molecules in the equatorial region of the uranyl dication in addition to the phosphorus-based ligand(s). The uranyl moiety is nonlinear in many of the complexes and coordination number (CN) 5 in the equatorial plane is the predominant binding motif. The phosphates are found to bind in both monodentate and bidentate binding modes depending on the charge and the number of water molecules. The $[UO_2(H_2PO_4)(H_2O)_n]^+$ complexes can accommodate up to three water molecules with the $H_2PO_4^-$ ligands remaining bidentate with a total equatorial CN of 5. $[UO_2(H_2PO_4)(H_2O)_4]^+$ has an equatorial CN of 5 with the phosphate ligand bound in a monodentate fashion, and a strong hydrogen bond between the H atom on an equatorial water and the terminal P=O group of $H_2PO_4^-$. In the $UO_2(HPO_4)(H_2O)_n$ complexes, protons can be abstracted from bound waters due to the increased negative charge on the HPO_4^{2-} ligand forming OH^- and $H_2PO_4^-$ ligands which separates the buildup of regions of negative charge. In $UO_2(HPO_4)(H_2O)_3$, the phosphate ligand is actually $H_2PO_4^-$ moiety bound in a monodentate fashion and results from the abstraction of a proton from a water forming a hydroxide ligand bound to uranium leading to CN 4. A hydrogen bond from the terminal P=O group to the H atom of a water stabilizes the monodentate mode. This hydrogen bond results in an elongated H-OH water bond and a 'hydroxide-like' interaction of this water with the uranyl center. In $UO_2(HPO_4)(H_2O)_4$, all of the ligands retain their identities. The HPO_4^{2-} ligand is bound in a bidentate fashion to the uranyl and three water molecules are bound in the remaining sites resulting in CN 5. The remaining water molecule is located in the second coordination sphere. Due to the steric effects of the second phosphate in the $UO_2(H_2PO_4)_2(H_2O)_n$ and $[UO_2(HPO_4)_2(H_2O)_n]^{2-}$ hydrated complexes ($n = 1 - 3$), fewer water molecules can be accommodated equatorially as compared to the monoligand complexes. Bidentate coordination modes for the phosphate ligands are more common. The structure of $UO_2(H_2PO_4)_2(H_2O)$ has bidentate $H_2PO_4^-$ ligands and a discrete bound water molecule resulting in the expected CN 5. The $UO_2(H_2PO_4)_2(H_2O)_3$ complex is structurally similar to the $UO_2(H_2PO_4)_2(H_2O)_2$ complex, with the exception both $H_2PO_4^-$ ligands are bound in a monodentate fashion. For the $[UO_2(HPO_4)_2(H_2O)_n]^{2-}$ ($n = 1$ and 3) complexes, the equatorial CN was found to be four rather than five with both complexes having at least one phosphate with monodentate binding. The $[UO_2(HPO_4)_2(H_2O)_2]^{2-}$ complex however, contains two bidentate HPO_4^{2-} with CN 6 and C_{2v} symmetry. In $[UO_2(HPO_4)_2(H_2O)_3]^{2-}$, both phosphate ligands exist as $H_2PO_4^-$ moieties with two hydroxide ligands bound to the uranyl. The hydroxides are hydrogen bonded to H atoms from the phosphate ligands and the remaining water acts as a second sphere water molecule hydrogen bonded to the hydroxide ligands. The $[UO_2(PO_4)(H_2O)_n]^-$ ($n = 1, 2$ and 4) complexes each have CN 4 and some bidentate phosphate binding as do the $[UO_2(PO_4)_2(H_2O)_n]^{4-}$ ($n = 1 - 2$) complexes. The (n = 3) complexes has CN 5 with the PO_4^{3-} ligand forming a bidentate bond to the uranyl dication. In $[UO_2(PO_4)_2(H_2O)]^{4-}$ both phosphate ligands are bidentate bound to the uranyl dication. In $[UO_2(PO_4)_2(H_2O)_2]^{4-}$, there is a proton transfer to a PO_4^{3-} ligand leading to the formation of an OH^- bonded to the UO_2^{2+}, a monodentate HPO_4^{2-} ligand and one bidentate PO_4^{3-} ligand.

The acidities of $H_xPO_4^{3-x}$ in $H_xPO_4^{3-x}(H_2O)_4$, x = 0-3 complexes were calculated with different SCRF models and compared to experiment. For the first deprotonation of H_3PO_4, all methods are within 2.4 pK_a unit of experiment with the exception of the MP2/aug-cc-pVDZ method which is within 4 pK_a units of experiment. For the second and third deprotonations of H_3PO_4, the

B3LYP/DZVP2 method predicts the pK_a's to increase linearly as found by experiment but the slope is too large and the pK_a's are in error by $\sim$ 5 and 10 pK_a units, respectively, as compared to experiment. The second pKa units are within $\sim$ 2 pK_a of experiment. The MP2/aug-cc-pVnZ (n = D, T, and Q) methods do not show a linear dependence for the pK_a's with the third pK_a within $\sim$ 6 pK_a units. The errors in the phosphate acidities can be reduced by using explicit waters of solvation. Our best predictions of the pK_a's for the different protonation states of phosphoric acid were obtained with a microsolvation approach with 4 explicit waters plus an implicit self consistent reaction field (SCRF). MP2/aug-cc-pVTZ was used for the gas phase values, and IEF-PCM with Pauling radii for the SCRF calculations. The first, second, and third acidities are within -1.9, -0.8, and -1.2 pK_a units of experiment, respectively.

The SCRF calculations were done with a variety of approaches and different SCRF approaches were found to optimal for different reaction types. Use of a hybrid microsolvation-continuum approach led to the prediction that $[H_2PO_4]^-$ will displace two H_2O molecule from $[UO_2(H_2PO_4)(H_2O)_3]^+$ to exothermically form neutral $[UO_2(H_2PO_4)_2(H_2O)]$. An additional $[H_2PO_4]^-$ will displace the remaining water to form the $[UO_2(H_2PO_4)_3]^-$ anion exothermically in solution. The addition of $[H_2PO_4]^-$ to $[UO_2(H_2PO_4)_2(H_2O)_3]$ with all three waters displaced is even more exothermic. HPO_4^{2-} will displace two waters from $[UO_2(HPO_4)(H_2O)_4]$ to form $[UO_2(HPO_4)_2(H_2O)_2]^{2-}$ exothermically. The binding of water molecules to the di-ligand complexes $UO_2(H_2PO_4)_2(H_2O)_n$, and $[UO_2(HPO_4)_2(H_2O)_n]^{2-}$, n = 1 – 4, was studied. Additional water molecules can cause the bonding of $H_2PO_4^-$ and HPO_4^{2-} to change from bidentate to monodentate exothermically while maintaining CN 5. This means that addition of water can generate a structure potentially capable of cross-linking to other uranyl phosphates to form the types of structures found in the solid state. $[UO_2(HPO_4)(H_2O)_3]$ is predicted to be a strong base in the gas phase and in aqueous solution and a moderate to weak acid in the gas phase and a very weak acid in solution. Our results show that one has to be careful in the type of solvent model that is used and also in the type of reaction to be used in the model. Different SCRF models perform differently for different types of reactions. Overall, the results show that it is possible to predict the energetic properties of aquo uranyl phosphate complexes using correlated molecular orbital theory in combination with SCRF approaches. The reaction energies derived from the DFT gas phase energies were not as reliable. The prediction of the solution energetics still requires the continued development of solvent modeling approaches as small changes in the models can lead to large changes in reaction energies in solution.

MgO Clusters

Interest in the geological sequestration of carbon dioxide, the principle anthropogenic greenhouse gas, has focused interest on magnesium-based minerals. Magnesium–based minerals are an important focus for geological sequestration studies because of their geological abundance and Mg oxides and hydroxides are very reactive with supercritical CO_2. In addition, MgO is the only engineered barrier material approved for emplacement in the Waste Isolation Pilot Plant (WIPP) in the U.S.

Global minima for $(MgO)_n$ structures were optimized using a tree growth – hybrid genetic algorithm developed in our group in conjunction with MNDO/MNDO/d semi-empirical molecular orbital calculations followed by density functional theory geometry optimizations with the B3LYP functional. High energy cubic and tubular isomers (including hexagonal, octagonal, and double hexagonal tubular isomers) were manually built and optimized to provide more information about high energy isomers. New lowest energy isomers were found for a number of $(MgO)_n$ clusters. The most stable isomers for $(MgO)_2$ and $(MgO)_3$ are planar and ring-like. For $(MgO)_n$, n > 3, the most stable isomers are all predicted to be 3-dimensional structures. These low energy 3-D structures are mainly cuboids, tubes, and polyhedrons, or their derivatives. The relative stability of these isomers changes as n increases, and also depends on whether n is a prime number. In the cases where n is a prime number, the highly ordered cubic and tubular geometries are not mathematically allowed for $(MgO)_n$, and the low energy clusters are usually defected or deformed cubic structures (e.g., structures for n = 13, 17, 23, and 29. For n < 20,

hexagonal tubular $(MgO)_n$ structures are more favored in energy than the cubic structures. The cubic structures and their variations dominate after n = 20. For the cubic isomers, increasing the size of the cluster in any dimension improves the stability. The effectiveness of increasing the size of the cluster in a specific dimension to improve stability diminishes as the size in that dimension increases. For cubic structures of the same size, the most compact cubic structure is expected to be the more stable cubic structure. The average Mg-O bond distance and coordination number both increase as n increases. The calculated average

Mg-O bond distance is slowly converging at n = 40 (2.055 Å) to the bulk value (2.106 Å). The average coordination numbers of the clusters also are converging to the bulk value (CN_{bulk} = 6), as

Figure 1. The average coordination number and bond distance (Å) for the lowest energy isomers of $(MgO)_n$.

the cubic structures start to become the dominant lowest energy isomers with CN = 4.6 for n = 40. (see Figure 1)

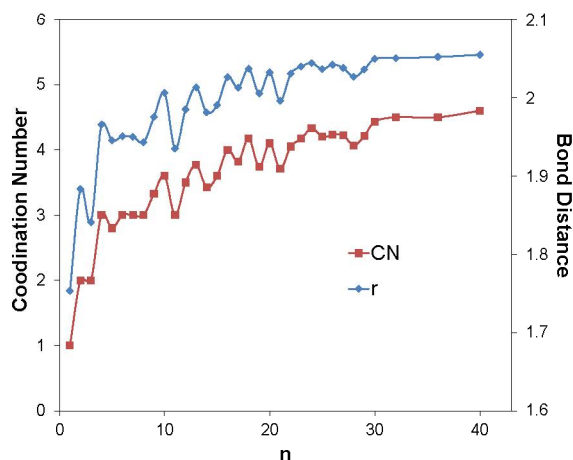The normalized clustering energy for $(MgO)_n$ are calculated from the expression

$$\Delta E(n) = E(MgO) - E((MgO)_n)/n \qquad (1)$$

For $(MgO)_n$, n = 2 - 8, the $\Delta E(n)$ calculated at the B3LYP/DZVP level were benchmarked with CCSD(T) values extrapolated to the complete basis set limit (cc-pVnZ, n = D, T, and Q). For n > 8, the $\Delta E(n)$'s were calculated at the B3LYP/DZVP level. The normalized clustering energies $\Delta E(n)$ for $(MgO)_n$, n = 2 – 8, were calculated at the B3LYP/DZVP and the CCSD(T)/CBS(DTQ) levels. The benchmark results show that, the $\Delta E(n)$'s calculated at the B3LYP/DZVP level are within 0.5 kcal/mol of the CCSD(T)/CBS predictions for the small $(MgO)_n$ clusters (n up to 8). Therefore B3LYP is a good functional to be used for the $\Delta E(n)$ calculations for larger $(MgO)_n$ clusters where CCSD(T) calculations are not feasible.

4

Figure 2 shows the normalized clustering energies of the cubic and tubular isomers for $(MgO)_n$ ($n \leq 40$). A larger value of a normalized clustering energy at the same n indicates better stability of an isomer. Figure 1 shows, for the structures in each cubic and tubular series, that the normalized clustering energy, which is an indicator of the isomer stability, increases as n increases. Vertical differences between the normalized clustering energy vs. n curves provide a comparison of the stability of the isomers from different series at the same value of n. It is found that the 3×4×m and 4×4×m cubic structures with m an integer have the best stability. The 2×4×m, 2×5×m, 2×6×m, and 3×3×m cub ic structures

Figure 2. Normalized clustering energies in kcal/mol v.s. n for the cubic and tubular structures.

shows comparable stability, and are less stable than the 3×4×m and 4×4×m cubic structures. Even less stable are the 2×3×m cubic structures, the hexagonal tubular structures and the octagonal tubular structures. The normalized clustering energy vs. n curve for the 2×2×m cubic structure series are below the curves for other cubic and tubular structure series, which suggests that the 2×2×m cubic structure series are the least stable among the series shown in Figure 2. For n < 20, the $(Mg_3O_3)_n$ and $(Mg_4O_4)_{n/4}$ tubular isomers show better stability than the cubic isomers, as most of the available cubic isomers are 2×2×m or 2×3×m. For example, the $(Mg_3O_3)_2$ hexagonal tubular isomer is 7 kcal/mol more stable than the 2×2×3 cubic structure for $(MgO)_6$. For $(MgO)_9$, $(MgO)_{12}$ and $(MgO)_{15}$, the hexagonal tubular structures are ~12 kcal/mol lower in energy than the cubic structures.
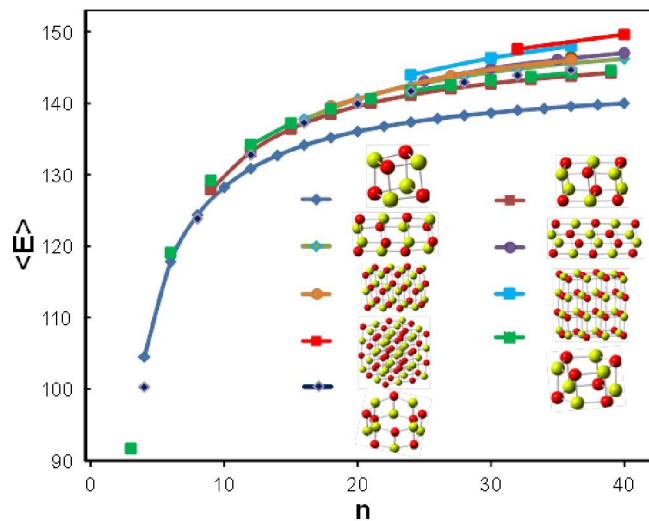
For the cubic isomers, increasing the size of the cluster in any dimension will raise the stability of the cluster. However, the effectiveness of increasing the size of the cluster in a dimension to gain stability diminishes as the size in that dimension increases, as the slopes of all of the normalized clustering energy vs. n curves decrease as n increases. Therefore, for cubic structure of the same size (with same n and volume), the most compact cubic structure (i.e., the structure where the sizes in the three dimensions are mostly comparable) is expected to be the more stable cubic structure. Therefore, even for large $(MgO)_n$ clusters where n is not a prime number(which means that cubic isomers can exist), the lowest energy isomers are not necessarily cubic (e.g., n = 26 and 27), when the cubic structures are not the most compact ones (2×2×m and 2×3×m cubic).

The $\Delta E(n)$ vs $n^{-1/3}$ curve is near linear for n > 4 (Figure 3). We do not expect the very small nanoclusters to have the same convergence to the bulk as do the larger structures as they are simply too small. The smaller clusters exhibit larger changes in the $\Delta E(n)$ as the amount of energy change as one monomer is added is spread over a smaller number of monomers. The intercept on the $\Delta E(n)$, the projected $\Delta E(n)$ value at $n \rightarrow \infty$, is predicted to be ~ 185 kcal/mol as we extrapolate the plot (n>4) by a linear function. The estimated value of $\Delta E(\infty)$ value from the

$\Delta E(n)$ vs $n^{-1/3}$ plot is expected to be slightly smaller than the intercept value, as the slope of the $\Delta E(n)$ vs $n^{-1/3}$ plot slightly decreases as $n^{-1/3}$ increases. The estimated value of ~185 kcal/mol is in good agreement with the bulk value of 176.9 kcal/mol, especially considering the slow variation in the energy for the larger clusters. Even at $n = 40$, the normalized clustering energy is still 26 kcal/mol below the bulk value. Even though the structures of $(MgO)_n$ and $(TiO_2)_n$ are quite different, the convergence of $\Delta E(n)$ of $(MgO)_n$ clusters is comparable to that for $(TiO_2)_n$ so this might provide a method to predict energies of the bulk in combination with accurate gas phase values of the monomer predicted using the Feller-Peterson-Dixon (FPD) method developed by us.
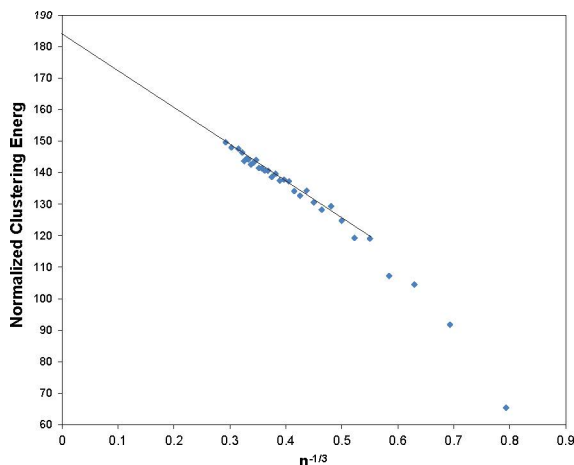

Figure 3. Normalized clustering energies vs (a) n and (b) $n^{-1/3}$ in kcal/mol for the lowest energy isomers of $(MgO)_n$.

The location of the HOMO and LUMO suggest that Lewis acids will bond to the oxygen and that Lewis bases will bind to the magnesium as expected. The most active atoms will be those on the corners. (Figure 4)

Structures and Energetics of (MgCO₃)ₙ NanoClusters

$MgCO_3$ minerals may play an important role in the mitigation of global warming, as $MgCO_3$ is the product of CO_2 capture reactions from aqueous Mg^{2+} or from mineral reactions. In many of these applications, changing the particle size can impact the mechanical, physical and chemical properties of $MgCO_3$, such as surface adsorption rate and catalytic reactivity, as a result of topological changes such as surface-volume ratio and density of the defect sites that vary with the particle size. There is substantial interest in the process of biomineralization, for example, the formation of amorphous calcium

Figure 4. Molecular orbital iso-surfaces for the HOMO and LUMO for $(MgO)_3$, $(MgO)_{21}$, and $(MgO)_{32}$.

carbonate, and it has been suggested that nanoclusters play a role in such processes. The structures of nanoclusters of magnesium carbonate clusters are of interest in terms of whether they can serve as precursors to the formation of amorphous magnesium carbonate. To understand the chemical processes of $MgCO_3$ that are affected by the particle size and to utilize the material more efficiently in different applications, the investigation of different particle sizes, especially nanoclusters, of $MgCO_3$ is important. Additionally, the reaction of MgO with CO_2 to form
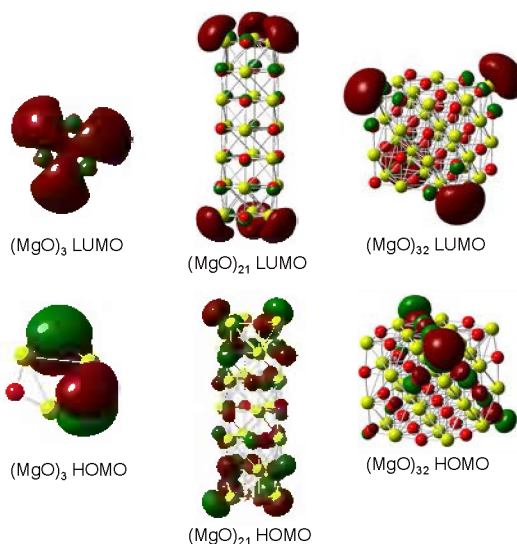
6

$MgCO_3$ is of interest, as this reaction is important to the CO_2 capture and long-term sequestration.

Global minima for $(MgCO_3)_n$ ($n \leq 16$) structures were optimized using a modified version of our tree growth - hybrid genetic algorithm (TG-HGA) in conjunction with MNDO/MNDO/d semi-empirical molecular orbital calculations followed by density functional theory geometry optimizations with the B3LYP functional. The most stable isomers for $(MgCO_3)_n$ ($n < 5$) are approximately 2-dimensional. Mg can be bonded to 1 or 2 O's of a CO_3 unit, forming Mg<O_2>CO or Mg-O-CO_2. The Mg-C distances in the Mg<O_2>C bonding scheme are ~ 0.5 Å shorter than the Mg-C distances in the Mg-O-CO_2 sites. The $(MgCO_3)_n$, $n = 1$- 4, clusters have Mg<O_2>CO sites exclusively. The Mg-O-CO_2 bonding scheme becomes favored as the cluster size increases. The average CN(C-Mg) increases as the cluster size n increases. The average CN(C-Mg) was calculated to be 5.2 for $(MgCO_3)_{16}$, slightly lower than the CN(C-Mg) of 6 in magnesite. For many of the nanoclusters, there are a number of energetically low-lying isomers, which may be present at equilibrium. Thus, continued nucleation could occur via different nanoclusters of the same size depending on the kinetics of the nucleation process.

The normalized reaction energies for the CO_2 dissociation reactions

$$(MgCO_3)_n \rightarrow (MgO)_n + n \ CO_2 \tag{2}$$

were calculated using equation (5),

$$<DE>(n)_{CO2} = E(CO_2) + (E((MgO)_n) - E((MgCO_3)_n)) / n \tag{3}$$

and the normalized CO_2 recombination energy $<RE>(n)_{CO2}$ for $(MgO)_n$ is the negative of $<DE>(n)_{CO2}$

$$<RE>(n)_{CO2} = - <DE>(n)_{CO2} \tag{6}$$

These values require an accurate value for the heat of formation of the $MgCO_3$ monomer which was calculated to be -111.8 kcal/mol at 298 K using the Feller-Peterson-Dixon (FPD) method

The normalized dissociation energy to form monomers increases as n increases. At n = 16, the normalized dissociation energy is calculated to be 116.2 kcal/mol, as compared to the bulk value of 154 kcal/mol. The bulk limit of <DE> was estimated from the experimental $\Delta H_f(298,s)$ and the calculated $\Delta H_f(298,g)$ for the monomer. The <DE> bulk limit can be obtained from the <DE> vs. $n^{-1/3}$ plot as the y-intercept of the extrapolated <DE> vs. $n^{-1/3}$ linear fit is the estimated <DE> value at $n^{-1/3} = 0$ (i.e. $n \rightarrow \infty$) (see Figure 5). The y-intercept is 152 kcal/mol, consistent with the estimated bulk value. The extrapolated <DE> vs. $n^{-1/3}$ linear fit can

Figure 5. Normalized $MgCO_3$ dissociation energy for $(MgCO_3)_n$ at the B3LYP/DZVP level vs $n^{-1/3}$.

be used to estimate the heat of formation of the bulk mineral and will help to provide bounds on

these values and to check the consistency of other types of calculations of the bulk thermodynamics, for example, the *ab initio* thermodynamic approach being developed by A. Chaka at PNNL.

The adiabatic reaction energies for the recombination reactions of $(MgO)_n$ clusters and CO_2 to form $(MgCO_3)_n$ were calculated. The exothermicity of the normalized recombination energy $<RE>_{CO2}$ decreases as n increases and converged to the experimental bulk limit rapidly. $<RE>_{CO2}$ was calculated to be -52.2 kcal/mol for the monomer and -30.7 kcal/mol for n = 16, as compared to the -27.9 kcal/mol for the solid phase reaction

The crystal structure of magnesite is layered with alternating layers of cations and anions and the Mg is an octahedral site with 6 oxygen atoms from 6 different CO_3^{2-} groups. The optimized nanoclusters do not exhibit this type of structure up to n = 16. Thus, one cannot readily cut a nanocluster out of the crystal, which is possible in some simpler metal oxides, such as MgO. As shown in Figure 6, structures for n = 4, 6, and 8 were cut from the crystal and then optimized. The results show that the clusters derived from the crystal structure are much higher in energy than those derived from the use of the TG-HGA. An issue with some of these structures is the presence of dangling C=O bonds, which cannot be eliminated without significant manual manipulation of the starting structure to overcome additional energy barriers. Thus the use of the TG-HGA or other approaches is important in generating optimal structures. For many of the clusters, multiple isomeric structures that are very close in energy were found. This suggests that

Figure 6. Optimized cluster structures for n = 4, 6, and 8 starting from initial clusters cut from the crystal. Energies in kcal/mol relative to the most stable structure for a given n

there may be complex equilibria for nanoclusters of the same number of $MgCO_3$ units and that detection of such nanoclusters could be complicated by the presence of more than one isomer with differing structures and spectroscopic signatures.
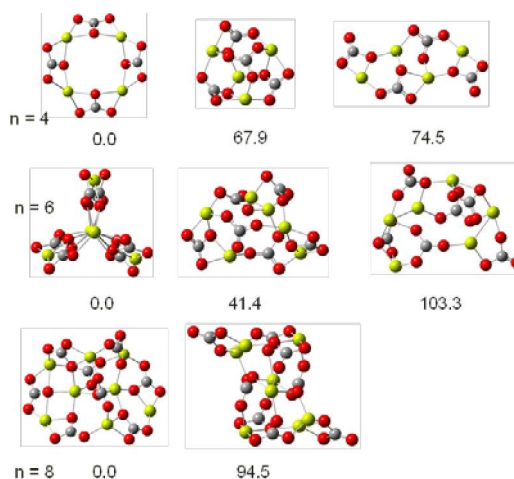
We also examined the process for loss of a CO_2 from $(MgCO_3)_{10}$ as shown in Figure 7. Loss of CO_2 generates an O^{2-} defect site and the loss of the CO_2 to generate this site requires only 12 kcal/mol ($\Delta H(0K)$). This initial observation will be pursued in future work to study the mechanism of decarboxylation of $MgCO_3$ clusters and subsequently minerals such as magnesite and nesquihonite.
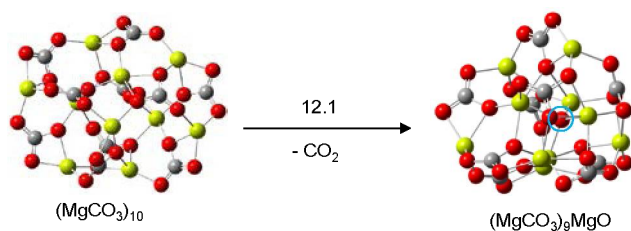

Figure 7. Formation of an O^{2-} defect site in $(MgCO_3)_{10}$. The O^{2-} site is circled in blue

The results suggest that the calculated clusters can serve as nucleation sites for the formation of amorphous magnesium carbonate analogous to the formation of amorphous calcium carbonate and its role in biomineralization. A long term goal of our effort is to understand the speciation of solutions containing $MgCO_3$. Our results show that the stable structures for the solid phases are not good guides to the structures of nanoclusters that may be present in solution. We thus calculated the vibrational frequencies for $(MgCO_3)_n$, and used our analysis of the results to interpret the major absorption bands in previous experimental IR studies for bulk magnesite. The calculated ^{13}C, ^{17}O, and ^{25}Mg chemical shifts together with the calculated vibrational spectra should be useful in identifying these clusters in solution.

CaO nanoclusters

We have extended our earlier work on MgO clusters to CaO nanoclusters using the same computational approach based on our TG-HGA technique for finding a global minimum. The results are similar to those obtained for the $(MgO)_n$ nanoclusters. The structures for each n are essentially the same as for $(MgO)_n$ except for n = 6, 8, 15, 21, and 28 where cubic structures are preferred over the non-cubic ones or more distorted structures found for $(MgO)_n$. The structures are similar to the MgO clusters and the low energy 3-D structures are mainly cuboids, tubes, and polyhedrons, or their derivatives with cuboids dominating for larger n. The Ca-O bond distance is shorter than the experimental value in the bulk by about 0.06 Å just as found for MgO. The average coordination numbers of the clusters are converging to the bulk value (CN_{bulk} = 6), as the condensed cubic clusters which are dominant forger n become large enough. The average CN is predicted to be 4.6 for the lowest energy $(CaO)_{40}$ isomer, which has 12 6-coordinate interior atoms and 68 surface atoms with lower coordination numbers, even though it has the same cubic structure as the bulk.

The CaO clustering energies at the B3LYP and M06 level were benchmarked against coupled cluster CCSD(T) calculations as shown in Table 1. The agreement of B3LYP with the CCSD(T) results is not as good as found for MgO clusters, but there is better agreement with the M06 functional.

Table 1. Benchmarks for the Normalized Clustering Energies in kcal/mol for $(CaO)_n$, n = 2 – 8 with the basis set for Ca = cc=pVnZ and for O = aug-cc-pVnZ.

n	CCSD(T)n =D	CCSD(T)n =T	CCSD(T)n =Q	CCSD(T) CBS	B3LYP n=T	M06 n = T
2	64.5	61.5	61.3	61.3	56.4	58.8
3	79.8	76.3	75.8	75.5	69.7	72.2
4	102.0	97.3	96.9	96.8	88.2	92.6
5	101.9	96.3	95.8	95.7	87.3	91.4
6	111.8	107.0	106.6	106.5	96.7	101.5
7	111.5	106.4			96.4	101.0
8	117.6	112.2			101.2	106.2

The plot of the normalized clustering energies $\Delta E(n)$ for $(CaO)_n$, n = 2 – 40 vs. $n^{-1/3}$ is shown in Figure 8. Extrapolating from n = 4, gives an intercept of 157 kcal/mol with the M06 DFTA functional, which is essentially the same as the value of 156 kcal/mol obtained from the

9

experimental ΔH_f of the solid and the FPD calculated value for the CaO gas phase molecule. The extrapolated DFT B3LYP value is 150 kcal/mol. In contrast, the same plot for MgO nanoclusters with B3LYP yields 185 kcal/mol with a best estimated value from experiment (solid MgO) and theory (MgO gas) of 177 kcal/mol. We are continuing to pursue this approach to estimate the heats of formation of the bulk to lower the error bars, as it is clear from the limited available data that the calculations do provide some bounds on the experimental values.
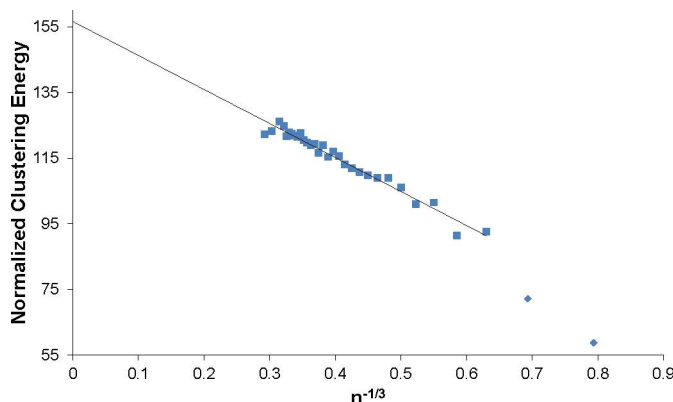

Figure 8. Normalized CaO dissociation energy for $(CaO)_n$ at the B3LYP/DZVP level vs $n^{-1/3}$.

The band gap in the CaO nanoclusters calculated from the HOMO-LUMO energy difference is around 4 eV for the cubic systems. This is about 3 eV below the value of 7.1 eV for the bulk from experiment but is only ~ 1 eV below the experimental band gap for thin films of CaO. The corresponding calculated band gap for the cubic MgO nanoclusters is ~5 eV as compared to the bulk experimental value of 7.8 eV. Thus the MgO nanoclusters have a larger band gap than the CaO nanoclusters consistent with the experimental difference for the bulk. We are exploring how these differences in the electronic structure of MgO and CaO nanoclusters affect their reactivity. We are also comparing their reactivity to that for other metal oxide nanoclusters that are being pursued in our catalysis work.

We are currently extending this work to $CaCO_3$ clusters to study the formation of amorphous calcium carbonate as well as the bulk crystal from prenucleation clusters.

pK$_a$'s of hydrated M^{2+} metal ions

The pK$_a$'s of metal dications (Table 2) have been predicted as an aid to our studies of geochemical reactions in solution. The acidities of $[Be(H_2O)_4]^{2+}$, $[M(H_2O)_6]^{2+}$, M = Mg^{2+}, Mn^{2+}, Fe^{2+}, Co^{2+}, Ni^{2+}, Cu^{2+}, Zn^{2+}, Cd^{2+}, and Hg^{2+}, and $[M(H_2O)_n]^{2+}$, M = Ca^{2+} and Sr^{2+}, n = 7 and 8 complexes have been predicted using density functional theory, second order Møller–Plesset perturbation theory (MP2) and coupled cluster CCSD(T) theory in the gas phase. pK$_a$'s in aqueous solution were predicted by using self-consistent reaction field (SCRF) calculations with different solvation models. Our computational study of the metal +2 complexes resulted in structures at the DFT/B3LYP level that are in reasonable agreement with the experimental ones. CN 6 is shown to be the most common binding motif for the majority of the metal +2 complexes, with each hexa-aquo cluster having reasonably high symmetry for the best arrangement of the water molecules in the first solvation shell. Be^{2+} adopts CN 4 whereas Sr^{2+} and Ca^{2+} adopt CN 7 or 8 in our calculations. Be^{2+} requires a second solvent shell for a reliable prediction of the pK$_a$. Most of the hexa-aquo clusters with CN 6 on loss of a proton retain CN 6 for $[M(H_2O)_5OH]^+$. $[Cu(H_2O)_5OH]^+$ has one water in the second solvation shell giving CN 5. The Group 12 $[M(H_2O)_5OH]^+$ (M = Zn^{2+}, Cd^{2+}, and Hg^{2+}) structures have similar CN 4 structures with C_s symmetry, where two waters are moved to the second solvation shell with each being stabilized

by six hydrogen bonds. Even though the two water molecules move into the second solvation shell, CN 6 with this $[M(H_2O)_5OH]^+$ structure still gives the best pK_a as compared to the CN 4 and 5 results.

Table 2. ΔG_{298} (gas, kcal/mol) and pK_a's of Metal/H_2O Complexes at the MP2/aug-cc-pVDZ(-PP) and CCSD(T)/aug-cc-pVDZ(-PP) levels.

M^{2+}/H_2O complex	MP2/CCSD(T) ΔG_{298}	MP2/CCSD(T) COSMO pK_a	MP2/CCSD(T) CPCM-COSMO-RS Radii pK_a	Expt pK_a
$[Be(H_2O)_4]^{2+}$	109.4/111.1	-6.0/-4.9	-3.9/-2.7	5.4
$[Be(H_2O)_4(H_2O)_8]^{2+}$	171.5/173.0	-0.2/0.8	0.7/1.7	5.4
$[Mg(H_2O)_6]^{2+}$	154.3/154.8	10.1/11.8	11.4/13.1	11.4, 11.2
$[Ca(H_2O)_7]^{2+}$	159.8/162.8	10.3/12.4	11.9/14.0	12.9, 12.7, 12.8
$[Ca(H_2O)_8]^{2+}$	162.7/165.9	9.5/11.8	10.7/13.0	12.9, 12.7, 12.8
$[Sr(H_2O)_7]^{2+}$	165.5/168.6	13.4/15.6	14.9/17.1	13.3, 13.2
$[Sr(H_2O)_8]^{2+}$	170.5/174.4	12.3/15.2	14.0/16.8	13.3, 13.2
$^6[Mn(H_2O)_6]^{2+}$	152.3/153.8	8.6/9.7	9.9/11.0	10.6, 11.0
$^5[Fe(H_2O)_6]^{2+}$	150.5/151.1	7.8/8.2	8.8/9.2	9.3, 9.5
$^4[Co(H_2O)_6]^{2+}$	147.0/150.7	4.3/7.0	5.2/7.9	9.7
$^3[Ni(H_2O)_6]^{2+}$	152.0/152.6	9.1/8.4	11.1/10.4	9.86
$^2[Cu(H_2O)_6]^{2+}$	148.7/148.1	7.7/7.2	8.6/8.2	8
$[Zn(H_2O)_6]^{2+}$	144.0/147.0	5.5/7.6	6.7/8.9	9.0
$[Cd(H_2O)_6]^{2+}$	154.5/156.9	9.4/11.1	10.8/12.6	10.0, 10.1
$[Hg(H_2O)_6]^{2+}$	145.0/146.7	1.6/2.9	2.7/4.0	3.4

The differences in the MP2 and CCSD(T) gas phase reaction free energies range from 0.5 to 3.9 kcal/mol, with the majority of the differences in free energy between the two methods less than 2.0 kcal/mol. The exceptions are found for the larger Ca^{2+} and Sr^{2+} complexes which exceed 2.9 kcal/mol. The predicted pK_a's using COSMO and CPCM with COSMO-RS radii agree best with the experimental values reported by Baes and Mesmer, Martell and Smith, and Hawkes at both the MP2/aug-cc-pVDZ and CCSD(T)/aug-cc-pVDZ levels of theory, with the CCSD(T) level of theory being the most accurate. Thus MP2 should be able to be used to predict the pK_a's with explicit waters included for larger systems as it is more cost effective scaling as N^5 for N basis functions with CCSD(T) scaling as N^7. The configuration sampling issue will be important for cluster models with more than one solvent shell and could become very costly even at the MP2 level with adequate basis sets.

The pK_a values predicted using the COSMO and CPCM with COSMO-RS radii solvation models and our single solvation shell model (excluding Be^{2+} and Al^{3+}) are in reasonable agreement with the experimental values. Each pK_a unit is 1.4 kcal/mol in free energy at 298 K, so in most cases, the error in the pK_a calculation is less than 3 kcal/mol in the free energy even though our model with only one solvent shell is being used with a continuum model for the remainder of the solvent. This is probably the best accuracy for absolute pK_a predictions that one can expect given a potential of an error on the order of 1 kcal/mol for the gas phase acidities, any error in the free energy of solvation of the proton, and an additional error of at least 1 kcal/mol

11

for the use of the SCRF. It is important to note that these are absolute values, not values relative to a standard. The use of a standard could potentially reduce the error in the predicted pK_a's.

We suggest that we can use this good agreement in the pK_a values with experiment to help assign the CN of the first solvation shell for the +2 atomic ions, which can be used to confirm the size of the first solvent shell obtained from EXAFS and XRD experiments in the absence of high energy x-ray scattering (HEXS) data. Thus the CN for Be^{2+} is the expected 4, although a second solvation shell is needed to obtain agreement with experiment for the pK_a due to the concentrated charge on the Be and the short Be-O bond distances. The most common CN for most of the remaining metal +2 ion complexes is 6. CN values of 7 and 8 cannot be distinguished for Ca^{2+} and Sr^{2+} based on the pK_a values and we suggest that both CN should be present in aqueous solution, consistent with the small energy differences between CN 7 plus a water and CN 8.

The Role of Managing Protons in Magnesite Formation

Qafoku and co-workers at PNNL have examined the precipitation products from reaction of $Mg(OH)_2$ in aqueous solutions saturated with supercritical CO_2 at high pressures (90 atm and 110 atm) and low temperatures (35 °C and 50 °C). They found that formation of magnesite was enhanced in sulfate-rich solutions, compared to chloride-rich solutions. On the basis of other work sponsored by the DOE BES Heavy Element Program, we developed a model based on the result that one of the key aspects during formation of solid phases by solution phase condensation reactions is the ability to accommodate the loss of protons from precipitate growth. In the case of magnesite growth, protons are generated during magnesite formation at elevated pCO_2 by reactions (1) and (2), for example.

$$Mg^{2+} + HCO_3^- \rightarrow MgCO_3 + H^+ \qquad\qquad (1)$$
$$Mg^{2+} + CO_2(aq) + H_2O \rightarrow MgCO_3 + 2H^+ \qquad\qquad (2)$$

At a molecular level, release of H^+ associated with forming $Mg\text{-}OCO_2$ bonds should be accompanied by removal of protons or additional bonds, and therefore ultimately magnesite, will not form. Conceptually, there are a variety of ways of accommodating protons generated during magnesite growth; at an initially high pH for example, by recombination with hydroxyl anions, the concentration of which is maintained by dissolution of basic minerals (forsterite, hydromagnesite, etc.). However, in the experimental study, the initial conditions with respect to Mg solid concentration were exactly the same except for the difference in counter-ion (Cl^- vs SO_4^{2-}) with the later accelerating magnesite formation. This suggests the possibility that the SO_4^{2-} counteranion can be effective in removal of protons due to formation of bisulfate ions (e.g. rxn 3)

$$Mg^{2+} + HCO_3^- + 2SO_4^{2-} \rightarrow MgCO_3 + 2HSO_4^- \qquad\qquad (3)$$

This reaction shows that, in the presence of high concentration of SO_4^{2-} and relatively low pH (similar to conditions of this study), magnesite nucleation and growth would be enhanced by HSO_4^- formation. Although the concentration of HSO_4^- would still be small at the pH value of the solutions (~5.5), the data here imply that acceleration of magnesite formation could occur in

the presence of polyprotic anions that can serve as proton sinks during magnesite nucleation and growth.

Potential Energy Surfaces for Carbonate Reactions

Portions of the potential energy surfaces for solvent (aqueous) displacement reactions involving the metal ions Mg^{2+} and Ca^{2+} with CO_2 and HCO_3^- have been calculated to better understand the energetics of these processes. H_2SiO_4 and $SiO(OH)_3^-$ are used as simple models for silicate minerals. The results in Table 3 show that CO_2 will not displace H_2O on Mg^{2+} complexes but that CO_2 will react with $Mg^{2+}(H_2O)_5OH$ to displace H_2O and form a bicarbonate complex. It is only slightly endothermic to displace $SiO(OH)_3^-$ by HCO_{3-} corresponding to the release of Mg^{2+} from a silicate surface. The reactions with Ca^{2+} (Table 4) show different behavior in terms of the energetics. For example, it is slightly exothermic to displace $SiO(OH)_3^-$ by HCO_3^- corresponding to the release of Ca^{2+} from a silicate surface.

Table 3. Energetics of the reactions of aqueous clusters of Mg^{2+} in the gas phase and in water in kcal/mol.

Reaction	ΔG_{Gas}	ΔG_{H2O}	pK_a
$Mg(H_2O)_6^{2+} \rightarrow Mg(H_2O)_5(OH)^+ + H^+$	153.0	16.4	12.0
$Mg(H_2O)_6^{2+} + CO_2 \rightarrow Mg(H_2O)_5(CO_2)^+ + H_2O$	16.0	9.5	
$Mg(H_2O)_5(OH)^+ + CO_2 \rightarrow Mg(H_2O)_5(OH)\cdot CO_2$	5.2	7.8	
$Mg(H_2O)_5(OH)\cdot CO_2^+ \rightarrow Mg(H_2O)_5(HCO_3)^+$	-6.9	-12.8	
$Mg(H_2O)_5(OH)^+ + CO_2 \rightarrow Mg(H_2O)_5(HCO_3)^+$	-1.7	-5.0	
$Mg(H_2O)_5(HCO_3)^+ \rightarrow Mg(H_2O)_4(HCO_3)^+ + H_2O$	3.9	-5.2	
$Mg(H_2O)_4(OH)^+ + CO_2 \rightarrow Mg(OH)(CO_2)(H_2O)_4^+$ (cis)	6.1	9.9	
$Mg(H_2O)_4(OH)^+ + CO_2 \rightarrow Mg(H_2O)_4(HCO_3)^+$	-1.9	-4.7	
$Mg(H_2O)_6^{2+} + Si(OH)_4 \rightarrow Mg(H_2O)_5(Si(OH)_4^{2+} + H_2O$	-11.7	6.0	
$Mg(H_2O)_5(Si(OH)_4^{2+} \rightarrow Mg(H_3SiO_4)(H_2O)_5^+ + H^+$	149.1	0.8	0.6
$Mg(H_3SiO_4)(H_2O)_5^+ \rightarrow Mg(H_2SiO_4)(H_2O)_5 + H^+$	272.1	17.6	12.9
$Mg(H_2O)_5(HCO_3)^+ \rightarrow Mg(HCO_3)(OH)(H_2O)_4 + H^+$	251.5	19.7	14.5
$HCO_3^- + Mg(H_2O)_5(OH)^+ \rightarrow OH^- + Mg(H_2O)_5(HCO_3)^+$	34.0	-0.5	
$HCO_3^- + Mg(SiO(OH)_3(H_2O)_5^+ \rightarrow SiO(OH)_3^- + Mg(H_2O)_5(HCO_3)^+$	12.9	1.6	

We have extended our previous studies of the reactions of water with CO_2 to from carbonic acid. In this case, the interest is in whether the presence of a metal ion will lower the reaction barrier for the reaction (Figures 9 and 10 and Tables 5 and 6). For the reaction of $CO_2(H_2O)_2$, the presence of the metal ion reduces the barrier. The barriers are reduced for the trimer for some of the reactants. Thus the metal may catalyze the proton transfer reaction.

Table 4. Energetics of the reactions of aqueous clusters of Ca^{2+} in the gas phase and in water in kcal/mol.

reaction	ΔG_{Gas}	ΔG_{H2O}	pK_a
$Ca(H_2O)_6^{2+} \rightarrow Ca(H_2O)_5(OH)^+ + H^+$	158.8	11.0	8.1
$Ca(H_2O)_6^{2+} + CO_2 \rightarrow Ca(H_2O)_5(CO_2)^+ + H_2O$	14.7	7.8	
$Ca(H_2O)_5(OH)^+ + CO_2 \rightarrow Ca(H_2O)_5(HCO_3)^+$	-4.0	-1.1	
$Ca(H_2O)_5(HCO_3)^+ \rightarrow Ca(H_2O)_4(HCO_3)^+ + H_2O$	7.3	-4.7	
$Ca(H_2O)_6(OH)^+ + CO_2 \rightarrow Ca(H_2O)_6(HCO_3)^+$	1.9	-1.2	
$Ca(H_2O)_6(HCO_3)^+ \rightarrow Ca(H_2O)_5(HCO_3)^+ + H_2O$	-3.0	-10.7	
$Ca(H_2O)_7(OH)^+ + CO_2 \rightarrow Ca(H_2O)_7(HCO_3)^+$	7.3	0.5	
$Ca(H_2O)_7(HCO_3)^+ \rightarrow Ca(H_2O)_6(HCO_3)^+ + H_2O$	-1.1	-8.8	
$Ca(H_2O)_6^{2+} + Si(OH)_4 \rightarrow Ca(H_2O)_5(Si(OH)_4^{2+} + H_2O$	-12.7	2.7	
$Ca(H_2O)_5(Si(OH)_4^{2+} \rightarrow Ca(H_3SiO_4)(H_2O)_5^+ + H^+$	158.1	5.9	4.3
$Ca(H_3SiO_4)(H_2O)_5^+ \rightarrow Ca(H_2SiO_4)(H_2O)_5 + H^+$	280.7	26.6	19.5
$HCO_3^- + Ca(H_2O)_5(OH)^+ \rightarrow OH^- + Ca(H_2O)_5(HCO_3)^+$	31.7	3.4	
$HCO_3^- + Ca(SiO(OH)_3(H_2O)_5^+ \rightarrow SiO(OH)_3^- + Ca(H_2O)_5(HCO_3)^+$	8.5	-1.5	
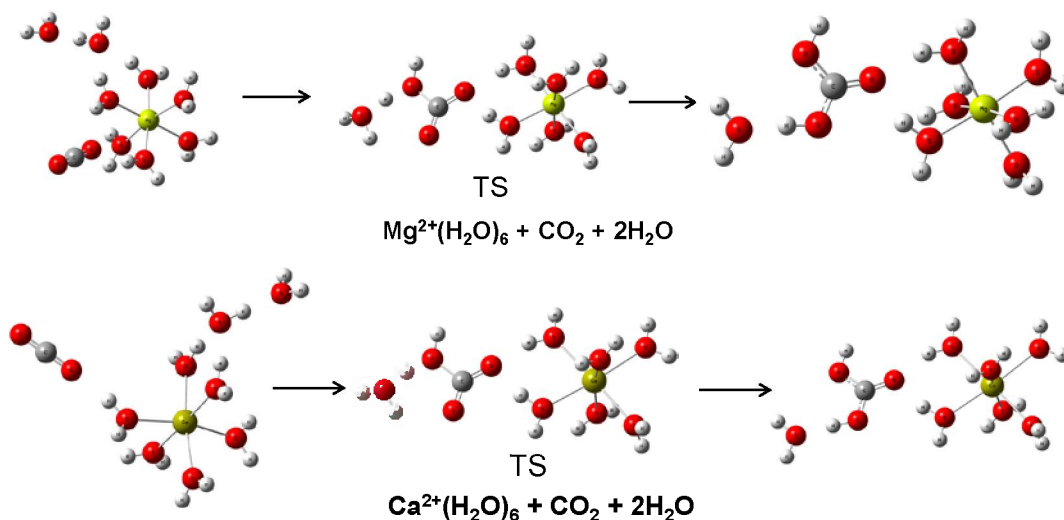
Figure 9. Reaction diagram of $M^{2+}(H_2O)_6 + CO_2(H_2O)_2$

Table 5. Reaction energetics in kcal/mol for $M^{2+}(H_2O)_6 + CO_2(H_2O)_2$

Structure	$\Delta H(0)_{gas,M^{2+}}$	$\Delta H(0)_{gas}$	$\Delta G(298)_{gas,M^{2+}}$	$\Delta G(298)_{gas}$	$\Delta G(298)_{aq,M^{2+}}$	$\Delta G(298)_{aq}$
$Mg^{2+}(H_2O)_6 + CO_2 + 2H_2O$						
TS	23.1	33.0	25.6	36.7	19.9	31.2
Product	3.4	8.6	4.7	10.9	2.6	6.5
$Ca^{2+}(H_2O)_6 + CO_2 + 2H_2O$						
TS	22.6	33.0	25.5	36.7	20.7	31.2
Product	2.7	8.6	4.2	10.9	3.0	6.5
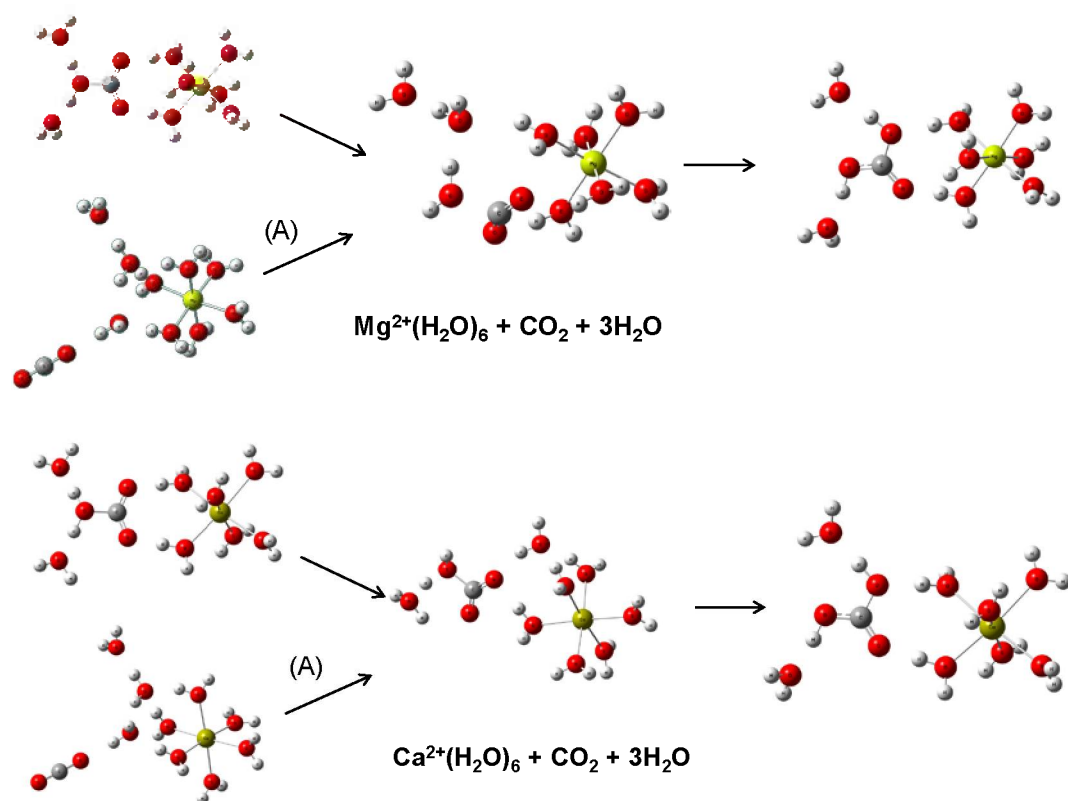
Figure 10. Reaction diagram of $M^{2+}(H_2O)_6 + CO_2(H_2O)_3$

Table 6. Reaction energetics in kcal/mol for $M^{2+}(H_2O)_6 + CO_2(H_2O)_3$

Structure	$\Delta H(0)_{gas,M^{2+}}$	$\Delta H(0)_{gas}$	$\Delta G(298)_{gas,M^{2+}}$	$\Delta G(298)_{gas}$	$\Delta G(298)_{aq,M^{2+}}$	$\Delta G(298)_{aq}$
$Mg^{2+}(H_2O)_6 + CO_2 + 3H_2O$						
TS	15.1	29.0	16.0	32.0	9.7	22.3
Product	-9.9	9.2	-10.7	10.4	-11.3	4.9
$Mg^{2+}(H_2O)_6 + CO_2 + 3H_2O$ (A)						
TS	28.3	29.0	30.2	32.0	22.6	22.3
Product	3.2	9.2	3.4	10.4	1.6	4.9
$Ca^{2+}(H_2O)_6 + CO_2 + 3H_2O$						
TS	7.1	29.0	10.0	32.0	8.5	22.3
Product	-11.5	9.2	-11.9	10.4	-12.2	4.9
$Ca^{2+}(H_2O)_6 + CO_2 + 3H_2O$ (A)						
TS	21.5	29.0	25.0	32.0	21.0	22.3
Product	2.9	9.2	3.1	10.4	0.3	4.9

15

NMR Chemical Shift Predictions

^{25}Mg and ^{13}C chemical shifts were calculated to determine if this method can be used to determine speciation in solution. All geometries were optimized at B3LYP level with DZVP for Mg and DZVP2 for other atoms. The ^{25}Mg chemical shifts in ppm (Table 7) were calculated relative to the standard $Mg^{2+}(H_2O)_6$ (shift absolute values: B3LYP/Ahlrichs VTZP = 581.0, ADF: BLYP/ TZ2P = 636.0, ADF: BLYP/TZ2P + ZORA = 637.6). The ^{13}C chemical shifts (Table 8) were calculated relative to the tetramethylsilane (TMS) standard (shift absolute values: B3LYP/Ahlrichs VTZP = 184.2, ADF: BLYP/ TZ2P = 179.9, ADF: BLYP/TZ2P + ZORA = 180.0) in ppm. The results suggest that it would be difficult to use the ^{25}Mg chemical shifts for speciation studies. The effects of scalar relativity were found to be small.

Table 7. ^{25}Mg chemical shifts in ppm

Molecule	B3LYP/VTZP	ADF: BLYP/ TZ2P	ADF: BLYP/TZ2P + ZORA
$[Mg(H_2O)_5(OH)]^+$	10.9	2.9	2.9
$[Mg(H_2O)(OH)_2, C_1$	44.7	14.1	14.0
$[Mg(H_2O)_2(OH)_2, C_2$	37.8	11.8	11.8
$[Mg(H_2O)_3(OH)_2, C_1$	28.5	8.7	8.7
$[Mg(H_2O)_4(OH)_2$	16.6	4.5	4.4
$Mg(CO_3), C_{2v}$	125.1	113.0	112.6
$[Mg(CO_3)_2]^{2-}, D_{2d}$	53.9	20.6	20.6
$Mg(CO_3)(H_2O)_4, C_2$	19.8	8.0	8.0
$[Mg(CO_3)_3]^{4-}, D_3$	1.0	1.1	1.1
$[Mg(CO_3)_2(H_2O)_2]^{2-}, C_2$	56.4	21.0	21.0
$[Mg(HCO_3)(H_2O)_4]^+$	10.7	4.3	4.3
$[Mg(HCO_3)(H_2O)_5]^+$	10.6	4.3	4.3
$Mg(HCO_3)_2, C_2$	30.8	11.0	11.0
$Mg(HCO_3)_2(H_2O)_2$	9.3	3.6	3.5
$Mg(HCO_3)_2(H_2O)_3$	22.4	9.3	9.3
$Mg(HCO_3)_2(H_2O)_4$	12.9	5.0	4.9
$[Mg(HCO_3)_3]^-$	5.8	0.9	0.9
$[Mg(HCO_3)_3(H_2O)]^-$	7.3	2.3	2.2
$[Mg(HCO_3)_3(H_2O)_2]^-$	19.5	6.7	6.6
$[Mg(HCO_3)_3(H_2O)_3]^-$	10.3	4.5	4.4
$Mg(HCO_3)(H_2O)(OH)$	34.6	11.7	11.7
$Mg(HCO_3)(H_2O)_2(OH)$	27.3	9.6	9.6
$Mg(HCO_3)(H_2O)_3(OH)$	15.3	5.5	5.4
$Mg(HCO_3)(H_2O)_4(OH)$	16.3	5.7	5.7

Table 8. ^{13}C chemical shifts in ppm

Molecule	B3LYP/ VTZP	ADF: BLYP/ TZ2P	ADF: BLYP/TZ2P + ZORA
$Mg(CO_3)$, C_{2v}	175.6	196.1	196.0
$[Mg(CO_3)_2]^{2-}$, D_{2d}	183.3	184.3	184.3
$Mg(CO_3)(H_2O)_4$, C_2	170.1	171.9	171.8
$[Mg(CO_3)_3]^{4-}$, D_3 (3)	188.7	188.7	188.7
$[Mg(CO_3)_2(H_2O)_2]^{2-}$, C_2	179.5	180.1	180.1
$[Mg(HCO_3)(H_2O)_4]^+$	180.0	179.7	179.6
$[Mg(HCO_3)(H_2O)_5]^+$	178.4	177.3	177.3
$Mg(HCO_3)_2$, C_2 (2)	181.9	181.4	181.2
$Mg(HCO_3)_2(H_2O)_2$	178.6	178.4	178.3
$Mg(HCO_3)_2(H_2O)_3$	177.5	176.7	176.5
$Mg(HCO_3)_2(H_2O)_3$	174.2	173.0	172.9
$Mg(HCO_3)_2(H_2O)_4$	173.3	173.2	173.2
$Mg(HCO_3)_2(H_2O)_4$	173.7	173.1	173.1
$[Mg(HCO_3)_3]^-$ (3)	175.8	175.7	175.7
$[Mg(HCO_3)_3(H_2O)]^-$	172.3	171.6	171.6
$[Mg(HCO_3)_3(H_2O)]^-$	175.6	175.4	175.4
$[Mg(HCO_3)_3(H_2O)]^-$	175.5	175.3	175.2
$[Mg(HCO_3)_3(H_2O)_2]^-$	172.0	171.6	171.5
$[Mg(HCO_3)_3(H_2O)_2]^-$	162.4	162.4	162.3
$[Mg(HCO_3)_3(H_2O)_2]^-$	173.0	171.8	171.7
$[Mg(HCO_3)_3(H_2O)_3]^-$	172.2	171.5	171.4
$[Mg(HCO_3)_3(H_2O)_3]^-$	161.4	161.3	161.2
$[Mg(HCO_3)_3(H_2O)_3]^-$	174.2	173.4	173.2
$Mg(HCO_3)(H_2O)(OH)$	180.8	180.4	180.3
$Mg(HCO_3)(H_2O)_2(OH)$	179.5	179.3	179.3
$Mg(HCO_3)(H_2O)_3(OH)$	178.6	178.4	178.4
$Mg(HCO_3)(H_2O)_4(OH)$ C	174.5	173.4	173.3

However, the ^{17}O NMR spectra were predicted to be able to provide insights into the chemistry. In collaboration with the experimental effort at PNNL led by J. Hu, the dissolution of $Mg(OH)_2$ in a water/scCO$_2$ system at 90 atm pressure and 50 °C was studied. The *in situ* ^{17}O NMR spectra allowed identification of various species that form in the water/scCO$_2$ system including dissolved CO_2 in the H_2O-rich phase, scCO$_2$, aqueous H_2O, and HCO_3^-. Evidence for the formation of polymeric Mg^{2+} clusters at high concentrations of Mg^{2+} in the H_2O-rich phase, a possible critical step needed for magnesium carbonate formation, was found. This work is being prepared for publication.

Publications

"High Level ab initio Predictions of the Energetics of $mCO_2 \cdot (H_2O)_n$ ($n = 1 - 3$, $m = 1 - 12$) Clusters" K. S. Thanthiriwatte, J. R. Duke, V. E. Jackson, A. R. Felmy, and D. A. Dixon, *J. Phys. Chem. A*, **2012**, *116*, 9718-9729.

"Near-Infrared Spectroscopic Investigation of Water in Supercritical CO_2 and the Effect of $CaCl_2$," Z. Wang, A. R. Felmy, C. J. Thompson, J. S. Loring, A. G. Joly, K. M. Rosso, H. T. Schaef, and D. A. Dixon, *Fluid Phase Equilibria*, **2013**, *338*, 155-163.

"Density Functional Theory Study of the Complexation of the Uranyl Dication with Anionic Phosphate Ligands with and without Water Molecules," V.E. Jackson, K. E. Gutowski, and D. A. Dixon, *J. Phys. Chem. A*, **2013**, *117*, 8939-8957

"Structures and Stabilities of $(MgO)_n$ Nanoclusters," by M. Chen, A. R. Felmy, and D. A. Dixon, *J. Phys. Chem. A*, **2014**, *118*, 3136–3146.

"Further Insights into the Structure and Chemistry of the Gilsonite Asphaltene from a Combined Theoretical and Experimental Approach," K. Li, M. Vasiliu, C. R. McAlpin, Yuan Yang, D. A. Dixon, K. J. Voorhees, M. Batzle, M. W. Liberatore, and A. M. Herring, *Fuel*, submitted, Nov. 2104

"Dynamics of Magnesite Formation at Low-Temperature and High-pCO_2 in Aqueous Solution," O. Qafoku, D. A. Dixon, K. M. Rosso, H. T. Schaef, M. E. Bowden, B. W. Arey, and A. R. Felmy, *Environ. Sci. Technol.* **2015**, *49*, 10736–10744

"Structures and Energetics of $(MgCO_3)_n$ Clusters, $n \leq 16$," M. Chen, V. E. Jackson, A. R. Felmy, and D. A. Dixon," *J. Phys. Chem. A*, **2015**, 119, 3419–3428

"The Prediction of the pK_a's of Aqueous Metal Ion +2 Complexes," V. E. Jackson, A. R. Felmy, and D. A. Dixon *J. Phys. Chem. A*, **2015**, *119*, 2926-2939.

Awards

Fellow, American Chemical Society, 2013. 1st member of ACS Geochemistry Division to be named an ACS Fellow.

2015, Distinguished Service Award, Division of Fluorine Chemistry, American Chemical Society

Presentations

Invited Lecture, *Recent Advances in Computational Fluorine Chemistry,* 21st Winter Fluorine Conference, St. Petersburg Beach, FL, Jan. 2013

Invited Lecture, *Computational Studies of Alternative Energy Systems,* Inaugural SEC Symposium, Renewable Energy, Atlanta GA, Feb., 2013

Invited Lecture, Tennessee Tech, *Computational Chemistry for Practical Applications,* Department of Chemistry, seminar, Cookeville, TN, Feb. 2013

Invited Lecture, *Computational Chemistry: Chemical Accuracy and Errors at Different Scales,* SIAM Conference on Parallel Processing for Scientific Computing, Boston MA, Feb. 2013.

Invited Lecture, *Computational studies of the properties of H_2O-CO_2 nanoclusters,* Division of Geochemistry, Symposium on Atomistic Computational Geochemistry: Atomic-Level Processes with Macroscopic Implications, 245th ACS National Meeting & Exposition, New Orleans, LA, April, 2013.

Invited Lecture, *Computational studies of hydrolysis reactions of CO_2 and actinides,* Session on "Theoretical and Experimental Approaches to Geochemical Reactions, Including Solvation, Complexation, Adsorption, and Redox," 2013 Goldschmidt Conference, Florence, Italy, August 2013.

Invited Lecture, *Reliable predictions of molecular properties for environmental studies,* Division of Environmental Chemistry, Symposium on Predicting Molecular Properties of Environmental Contaminants: Empirical and Theoretical Methods 246th ACS National Meeting, Indianopolis, In, Sept. 2013

Keynote Lecture, *Why Computational Actinide Chemistry Needs Flops (& Memory & Interconnect & Disk),* ORNL User meeting July 2014

Invited lecture, *Computational studies of metal (including actinides) and main group fluorides and oxides,* International Conference on Theoretical and High Performance Computational Chemistry-2014, Beijing China, Sept. 2014.

Invited Lecture, *Computational studies of fluorine containing molecules,* 22nd Winter Fluorine Conference, St. Petersburg Beach, FL, Jan. 2015.

Invited Lecture, *Computational studies of fluorine containing molecules,* Division of Fluorine Chemistry, Fluorine Award Symposium, 249th ACS National Meeting, Denver, March 2105

Invited Lecture, *Computational Studies of Iodo Compounds (Adventures in The Physical Chemistry of I),* Division of Fluorine Chemistry, Iodine Award Symposium, 249th ACS National Meeting, Denver, March 2105

Invited Lecture, *Using Computational Chemistry to Address Problems in Energy and the Environment,* Rimes Lecture, Springhill College, Mobile AL, April, 2015

Invited Lecture, *Computational Actinide Chemistry,* 2015 SETCA Annual Meeting, University of Central Florida, May 14-16, 2015

Invited Lecture, *Prediction of pK$_a$'s and Acidities of Organic and Inorganic Acids*, Division of Computational Chemistry, 250th ACS National Meeting, Boston, August 2015

Invited Plenary Lecture, *Challenges of Developing Computational Chemistry Software for Massively Parallel Computers*, DOE High Performance Computing Operational Review (HPCOR) on Scientific Software Architecture for Portability and Performance, Gaithersburg. MD, Sept. 2015